Supplementary Information

Solvated Pyromellitic Acid-Modified Separator for Stable Lithium Metal Anodes and High-Performance Li-S Batteries

Jing Zhang, [a] Yi Feng,*[a] Yun-Dong Cao, [a] Lin-Lin Fan,*[a] Cai-Li Lv, [a] Lei Cheng, [b] Guang-Gang Gao [a] and Hong Liu*[a]

a.School of Materials Science and Engineering, University of Jinan, Jinan, 250022, P. R. China.

b.Shandong Qinlu Energy Technology Co., Ltd, Jinan, 250022, P. R. China.

*Corresponding authors. E-mail address: mse_fengy@ujn.edu.cn (Yi Feng), mse_fanll@ujn.edu.cn (Lin-Lin Fan), mse_liuh@ujn.edu.cn (Hong Liu).

1. Material characterization

The microstructures and elemental mapping of PMA-DMAc modified separators were obtained via scanning electron microscope (SEM, Zeiss, Gemini 300) equipped with X-ray energy dispersive spectroscopes (Oxford, X-Max^N 50). X-ray diffraction (XRD) was detected by Rigaku SmartLab 9KW. X-ray photoelectron spectrometer (XPS) was recorded on an ESCA Lab MKII X-ray photoelectron spectrometer with non-monochromatized Mg Kα X-rays as the excitation source. Fourier transform infrared spectroscopy (FTIR) was obtained using a NEXUS-870 spectrophotometer with KBr pellets. Contact angles were detected by a POWERREACH JC2000D2G instrument. Ultraviolet-visible (UV-Vis) measurement was performed by SHIMADZU UV-3600 spectrometer within the wavelength range of 200-600 nm. Raman spectroscopy employed a Raman spectrometer (Labramis, Horiba Jobbin Yvon, Paris, France) with a wavelength of 532 nm. The diffraction data were collected on a Rigaku XtaLAB Synergy diffractometer with Mo Kα radiation (λ = 0.71073 Å). The intensity data were scaled and corrected for absorption, and final cell constants were calculated from the xyz centroids of strong reflections from the actual data collections after integration. The space group was determined based on systematic absences and intensity statistics. The structure was solved using the charge-flipping algorithm, as implemented in the program SUPERFLIP2 and refined by full-matrix least-squares techniques against F2 using the programs SHELXS 2018/2 and SHELXL 2019/3 within OLEX2 1.5.[1] All nonhydrogen atoms were refined anisotropically, and the hydrogen atoms were included at idealized positions. The SQUEEZE option of PLATON was used at the final refinement to account for the contribution of disordered solvent molecules to the calculated structure factors.[2] Other non-hydrogen atoms were found in alternating difference Fourier syntheses and least-squares refinement cycles. During the final

cycles, except for some solvent molecules, all other non-hydrogen atoms were refined anisotropically. Hydrogen atoms were placed in calculated positions refined using idealized geometries and assigned fixed isotropic displacement parameters. The joint Cambridge Crystallographic Data Center (CCDC) number of 2506260 for PMA-DMAc.

2. Electrochemical measurement

DH7006 electrochemical workstation (Jiangsu Donghua Analytical Instrument Co., Ltd, Donghua Analytical) was used to test cyclic voltammetry (CV) and electrochemical impedance spectroscopy (EIS). The cycle performance, rate performance tests, and galvanostatic intermittent titration technique (GITT) test of Li-S cells, as well as cycle performance and rate performance tests of Li//Li symmetric cells were carried out on the Neware battery test system (CT-4008-5V50mA-164, Shenzhen Neware Electronics Co., Ltd., China).

3. Part of the formula

3.1 The ionic conductivity (σ)

The ionic conductivity of the separator was tested with two stainless steels (SS) blocking cells (SS//separator//SS) by EIS in the frequency range from 1000 kHz to 0.01 Hz on the electrochemical workstation. The ionic conductivity was calculated according to the following equation:

$$\sigma = \frac{d}{R_b S} \#(S1)$$

where d is the thickness of the separator, R_b and S represent the bulk resistance and the effective area of the separator, respectively.

t_{Li^+} is the lithium transfer number, and the value is calculated as follows：

$$t_{Li+} = \frac{I_S(\Delta V - I_0 R_0)}{I_0(\Delta V - I_S R_S)} \#(S2)$$

R_0 and R_s refer to the interfacial resistance before and after AC impedance. I_0 and I_s represent the current value in initial and steady state under a polarization potential of 10 mV.

3.2 The quantitative imaging framework for lithium morphology

The calculation analysis was based on lithium metal symmetric cells cycled for 100 h under 1 mA cm^{-2} and 1 mAh cm^{-2}. Three representative SEM images of the cycled lithium anodes were respectively collected from cells using the pristine PP separator and the PMA-DMAc/PP separator for calculation analysis. The analysis followed rigorous and reproducible steps, with key parameter optimizations to enhance precision:[3]

(1) Image standardization and refined binarization processing

To thoroughly eliminate bias from subjective threshold selection and accurately capture morphological details, a systematic threshold-scan binarization of all SEM images was performed. Specifically, for each grayscale image, binarization was iteratively performed starting from a brightness threshold of 0.1, increasing in steps of 0.05 up to 0.95. In order to facilitate presentation, the Fig. S15-20 show an iterative binarization process starting at a brightness threshold of 0.1 and increasing in steps of 0.10 up to 0.90. This process ensures that the optimal binarized state, which most authentically represents the topological features of lithium deposition, can be identified regardless of the original image contrast.

(2) High spatial resolution uniformity calculation

Each image is divided into a number of quintiles, q. For each binarization result, images show the total number of white pixels (A_{white}) representative of the boundaries between

lithium particles and the total number of pixels within each slice (A_{total}), divided into 25 slices (outlined in red) for the calculation of Index of Dispersion (ID). Each of the 25 slices contains 25 pixels. The meaning of $\{x_1, x_2, \cdots x_q\}$ and x is adapted to represent the fractional coverage of Li (FC_i) and the average fractional coverage of Li among all quadrats or slices (FC_{avg}).

(3) Determining the optimal index of dispersion for a single image

Based on the aforementioned 25 FC_i values, the ID value for each threshold was calculated according to the formula:

$$ID = \frac{(q-1)s^2}{FC_{avg}}, \#(S3)$$

$$where\ s = \sqrt{\frac{\sum (FC_i - FC_{avg})^2}{q}}, FC_i = \frac{A_{white}}{A_{total}}.$$

After calculations for all thresholds (0.1 to 0.95) were completed, the maximum ID value was selected as the final ID for that SEM image. This "maximum ID criterion" aims to standardize contrast differences between images, ensuring that all comparisons are based on an equally stringent foundation of morphological identification.

(4) Obtaining statistically reliable sample-level conclusions

For both the pristine PP separator group and the PMA-DMAc/PP separator group, the average of the ID values from the three images in each group was calculated to obtain the sample ID (SID), serving as the core quantitative metric for deposition uniformity. The SID was calculated as the average ID across the total number of individual images (P_{images}) for each sample.

$$SID = \frac{1}{P_{images}} * \sum_{1}^{P} ID_1 + ID_2 + ID_3 + \ldots + ID_P. \#(S4)$$

3.3 Density functional theory (DFT) calculations

The calculations were performed within the framework of DFT, by using the projector augmented wave method as implemented in the Vienna ab Initio Simulation Package. The exchange-correlation energy was in the form of Perdew-Bruke-Ernzerhof. The cutoff energy for the plane-wave basis set was 500 eV, and 2×2×1 Γ-centered k-point grids were used for the Brillouin zone integrations. For the surface systems, the bottom atom layers were fixed to simulate the body state, while the top atom layers were free to simulate the surface state. To reduce the interactions between each surface, a vacuum of 20 Å was contained in our calculation models. All structures were fully relaxed to the optimized geometry with the force convergence set at 0.01 eV/Å. To investigate the lowest energy configurations of adsorbed systems, we carefully manipulated structure parameters of the initial state (the distance, angle, and displacement between molecule and surface) to fully relax and selected the lowest energy result as the final state. The binding energy (E_{ads}) of lithium adsorbing on the substrate materials is calculated referring to the following equation:

$$E_{ads} = E_{total} - E_{substrate\ materials} - E_{Li} \#(S5)$$

where E_{total} is the total energy of substrate materials combined with lithium, $E_{substrate\ materials}$ is the surface energy of PMA and DMAc, E_{Li} represents the energy of lithium in vacuum.

3.4 Galvanostatic intermittent titration technique (GITT) test

Before testing, the cells were rested under open circuit voltage for 12 h. The specific procedures were as follows: a 0.1 C current pulse was applied for 20 min, followed by 30 mins rest relaxation process. The polarization during electrochemical operation was quantified by introducing both internal resistance parameters and the Li^+ diffusion coefficients, with their correlation mechanisms described as follows:

$$\Delta R_{internal} = \frac{|\Delta_{QOCV-CCV}|}{I_{applied}} \#\ (S6)$$

Where ΔV is the voltage difference between the quasi-open circuit voltage (QOCV) and the closed circuit voltage (CCV), and $I_{applied}$ is the applied current.

3.5 CV at multiple scan rates test

CV at multiple scan rates were tested under 0.1, 0.2, 0.4, 0.6, and 0.8 mV s^{-1} after 8 h rest under open circuit voltage. The Randles-Sevcik equation is used to determine the lithium-ion diffusion coefficient:

$$I_p = 2.69 \times 10^5 n^{\frac{3}{2}} A D^{\frac{1}{2}} C v^{\frac{1}{2}} \#(S7)$$

In the given equation, the variables I_p, n, A, D, C, and v denote the peak current, charge transfer number, active electrode surface area, diffusion coefficient of lithium ions, concentration of lithium ions in the solution, and the scan rate, respectively.

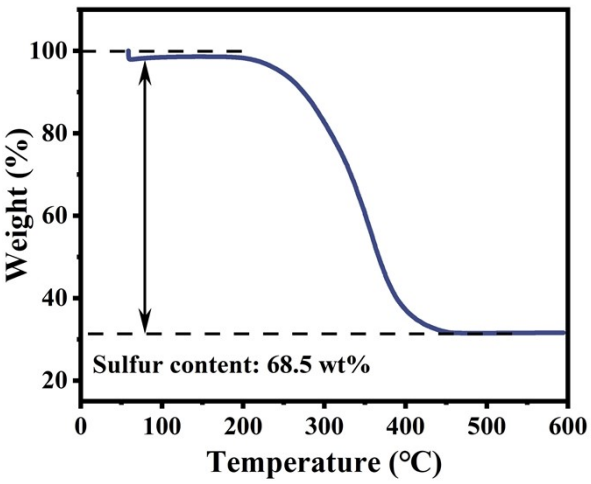

Fig. S1 TGA curve of C/S for cathode.

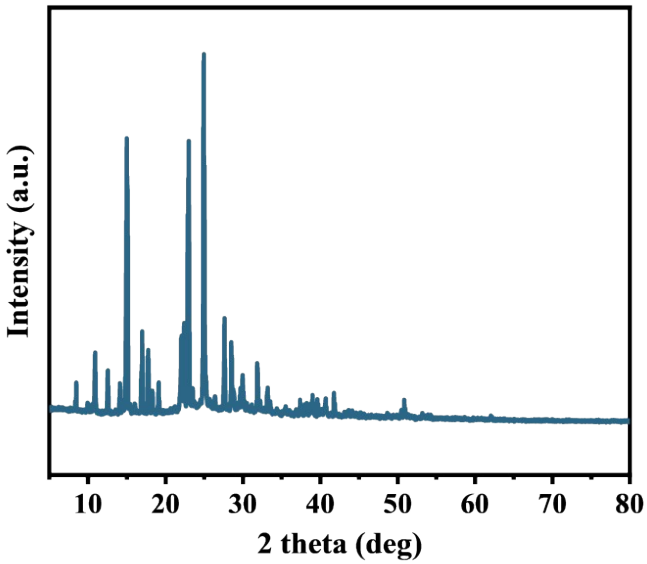

Fig. S2 XRD pattern of PMA-DMAc.

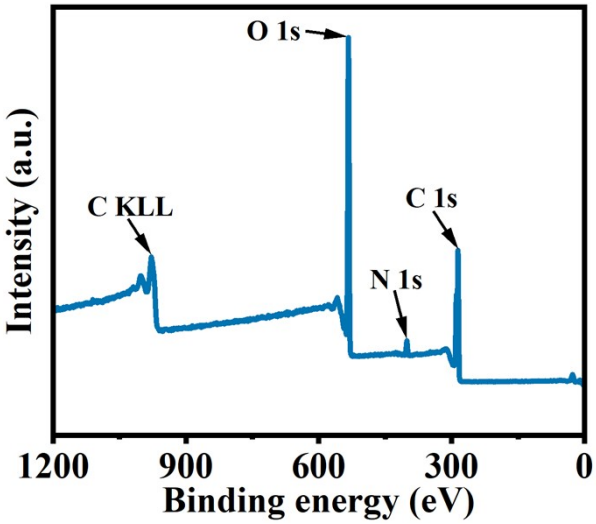

Fig. S3 Full XPS spectra of PMA-DMAc.

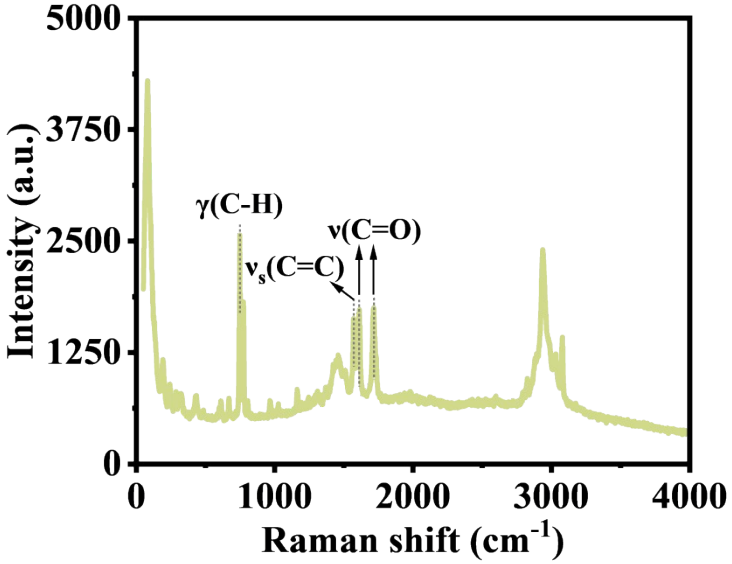

Fig. S4 Raman spectra of PMA-DMAc.

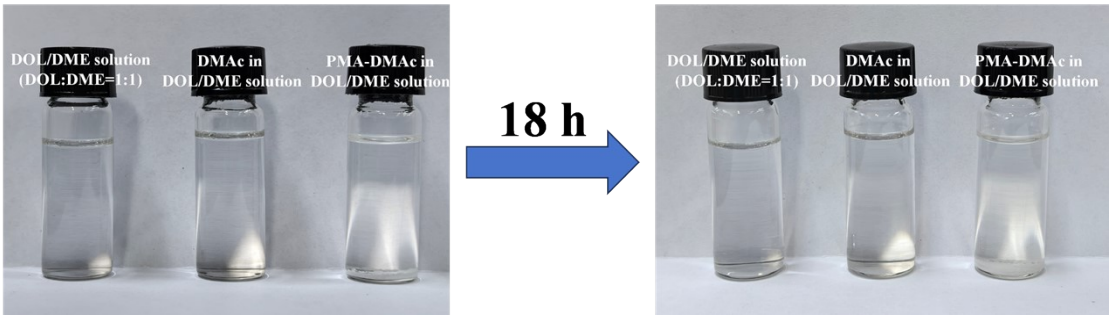

Fig. S5 Observation of solubility of DMAc and PMA-DMAc powder in DOL/DME solution.

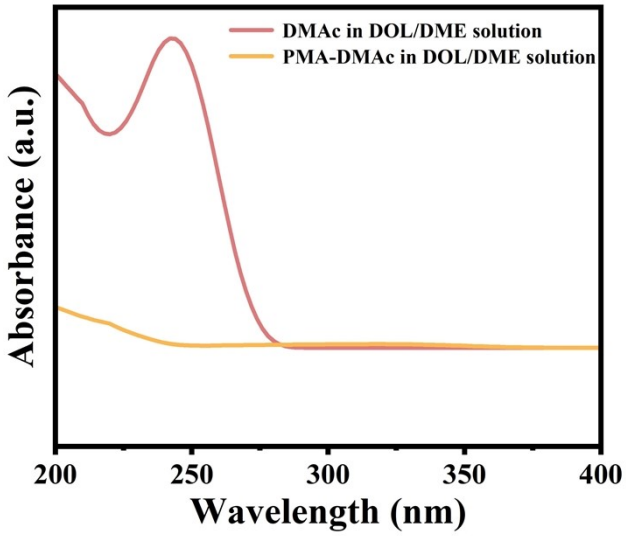

Fig. S6 UV-vis spectra of the supernatants of the solutions containing PMA-DMAc powder and DMAc.

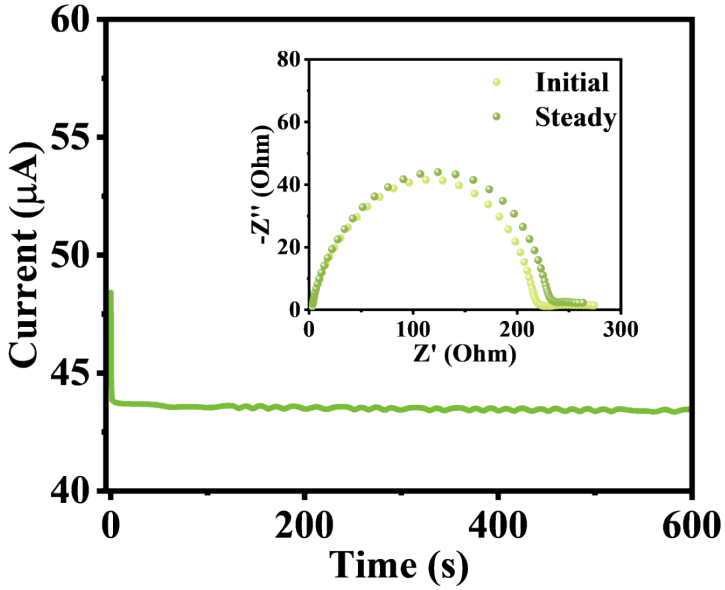

Fig. S7 Measurement of t_{Li}^{+} using potentiostatic polarization of Li//Li symmetric cell with pristine PP separator (inset: Nyquist plots of impedance before and after polarization).

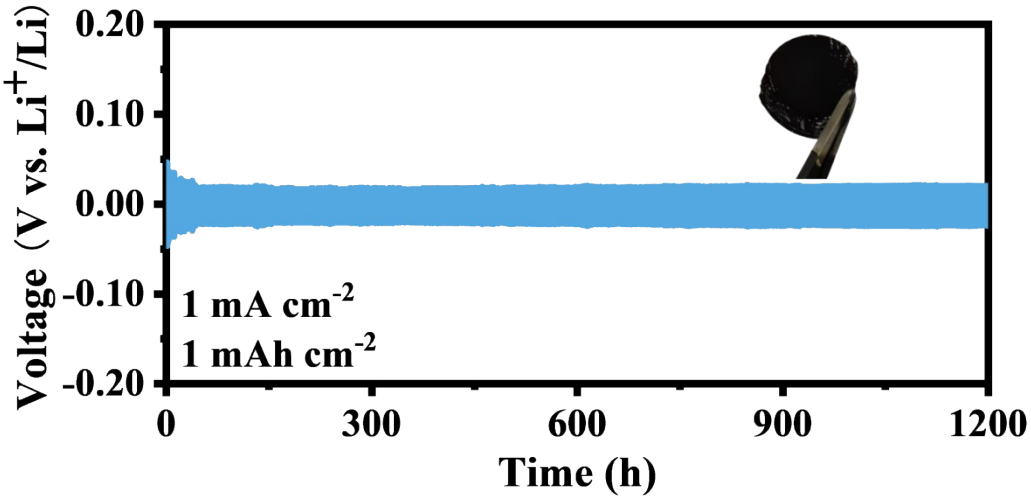

Fig. S8 Galvanostatic cycling of Li//Li symmetric cell with PMA-DMAc/PP separator at 1 mA cm^{-2} with areal capacity of 1 mAh cm^{-2} (inset: digital photograph of the PMA-DMAc/PP separator after cycling).

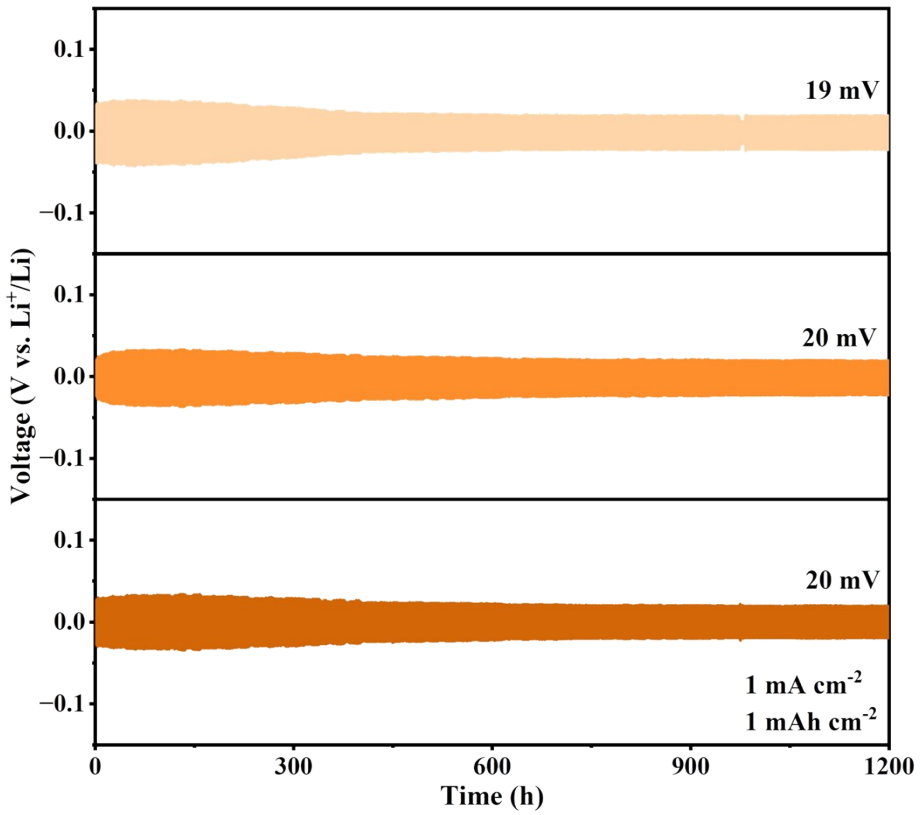

Fig. S9 Galvanostatic cycling of Li//Li symmetric cells with PMA-DMAc/PP separators at 1 mA cm^{-2} with areal capacity of 1 mAh cm^{-2} for three independent cells.

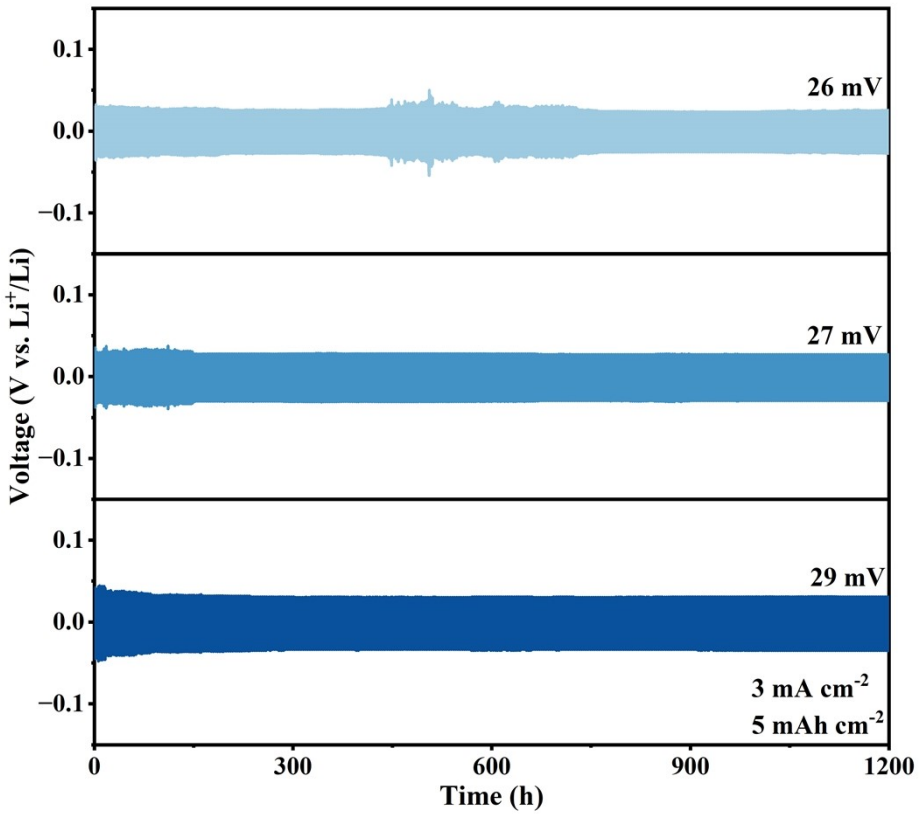

Fig. S10 Galvanostatic cycling of Li//Li symmetric cells with PMA-DMAc/PP separators at 3 mA cm^{-2} with areal capacity of 5 mAh cm^{-2} for three independent cells.

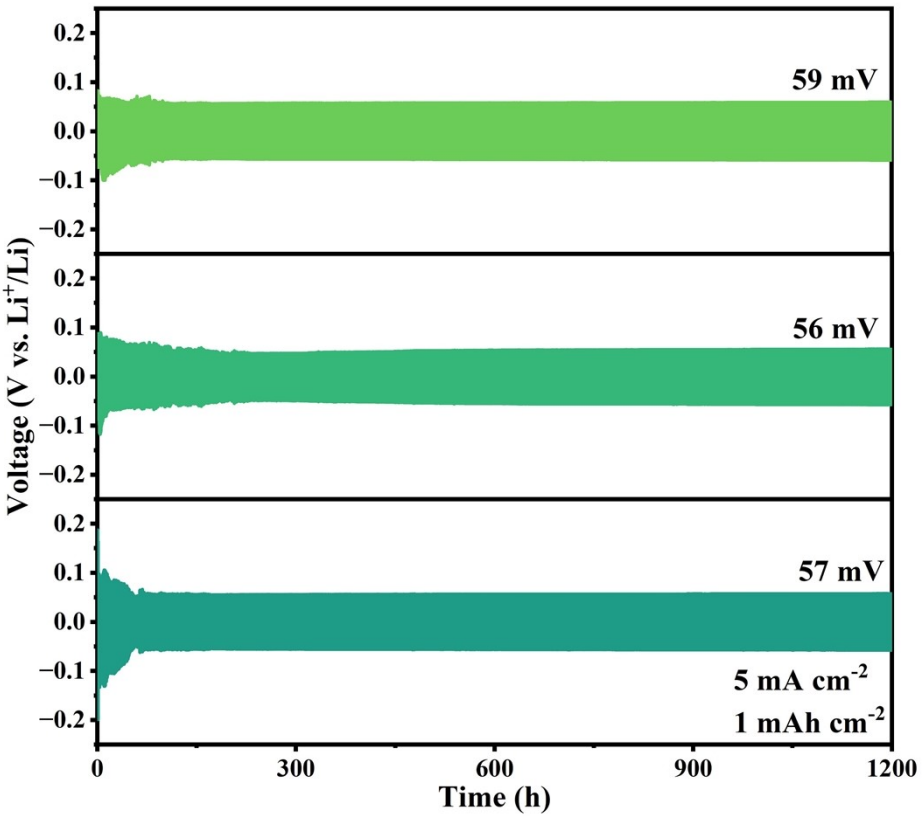

Fig. S11 Galvanostatic cycling of Li//Li symmetric cells with PMA-DMAc/PP separators at 5 mA cm^{-2} with areal capacity of 1 mAh cm^{-2} for three independent cells.

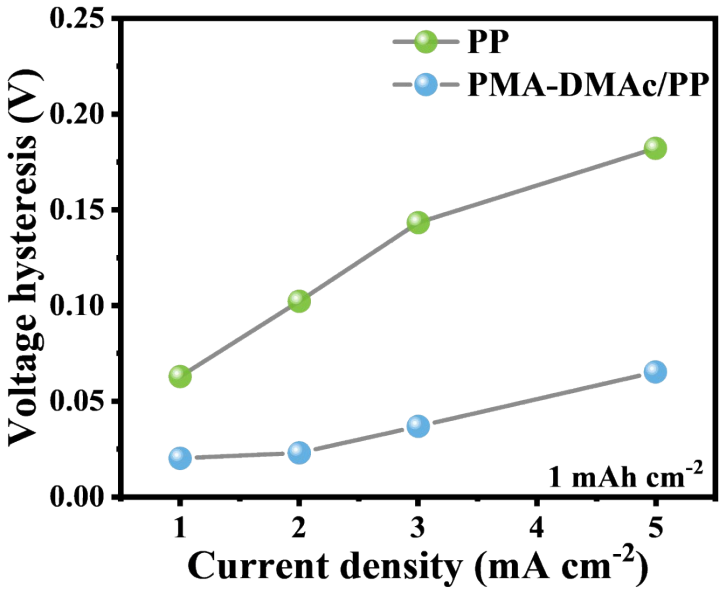

Fig. S12 Voltage hysteresis of Li//Li symmetric cells with different separators at 1, 2, 3, and 5 mA cm^{-2}.

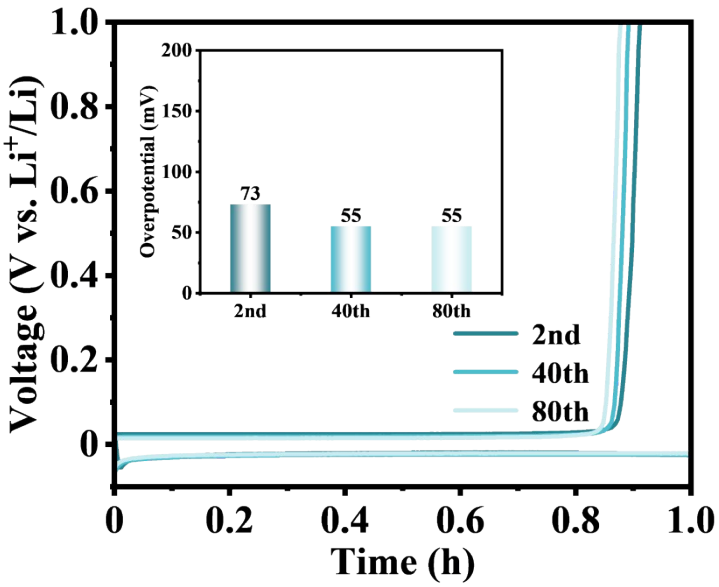

Fig. S13 Voltage profiles of the lithium plating and stripping process for Li//Cu cells with PMA-DMAc/PP separator at 1 mA cm^{-2} with areal capacity of 1 mAh cm^{-2}.

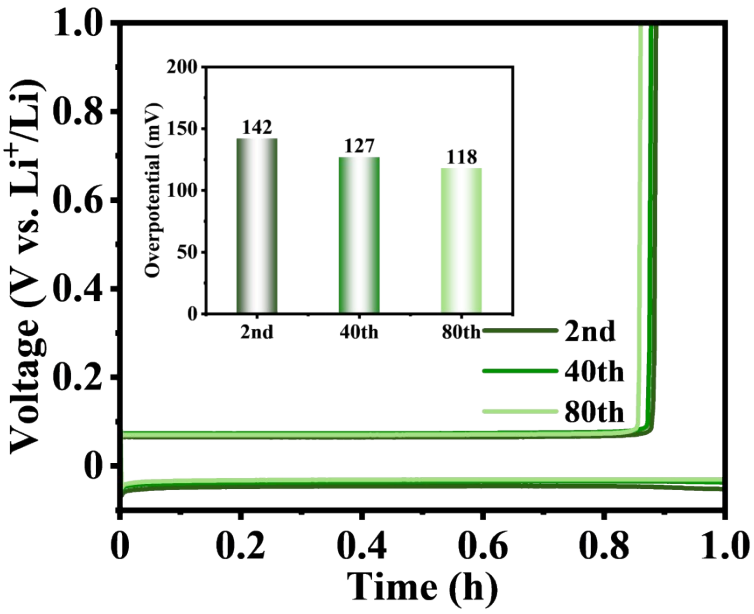

Fig. S14 Voltage profiles of the lithium plating and stripping process for Li//Cu cells with pristine PP separator at 1 mA cm^{-2} with areal capacity of 1 mAh cm^{-2}.

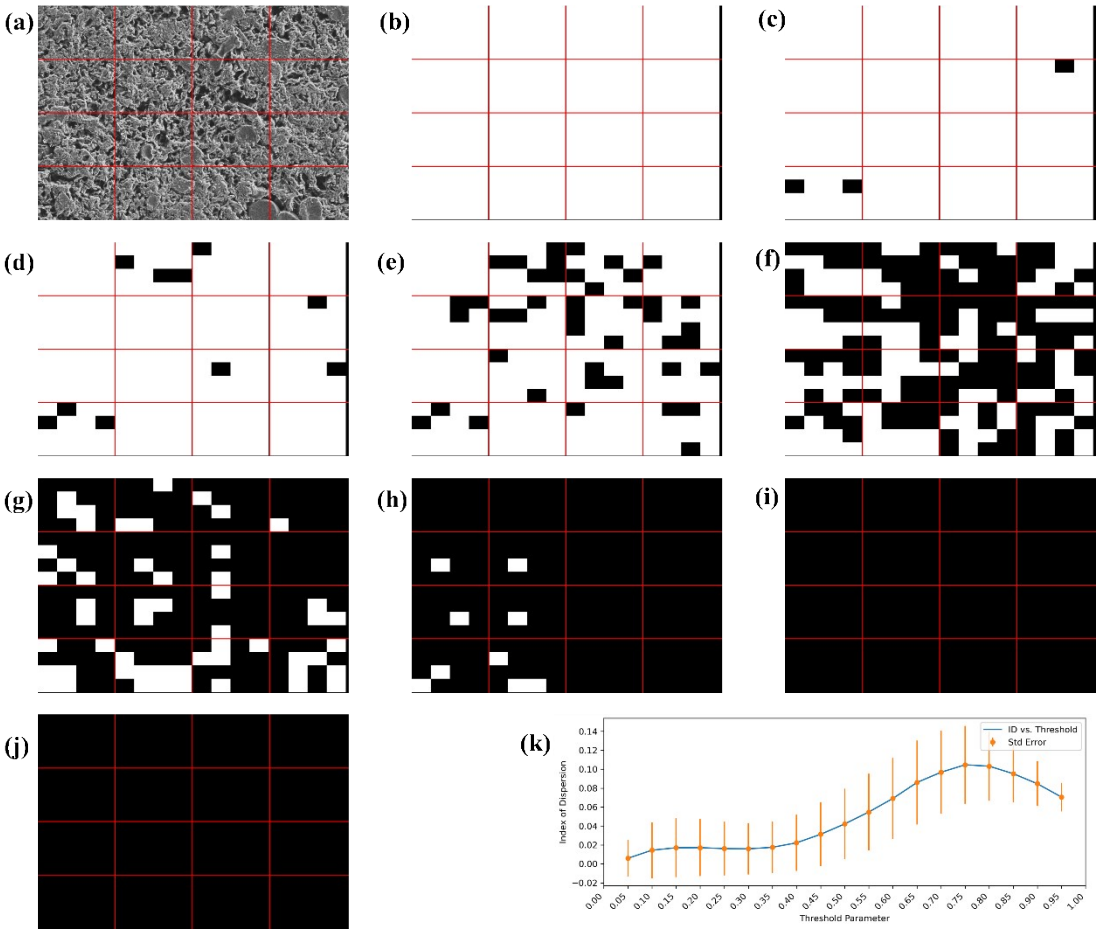

Fig. S15 (a) The SEM image 1 of the surface of lithium foil with PP separator at 100 h lithium plating under 1 mA cm^{-2} and 1 mAh cm^{-2}. (b-j) Binarization is iteratively performed starting from brightness threshold of 0.1, increasing in steps of 0.10 up to 0.90. (k) ID plotted for lithium deposition at these conditions.

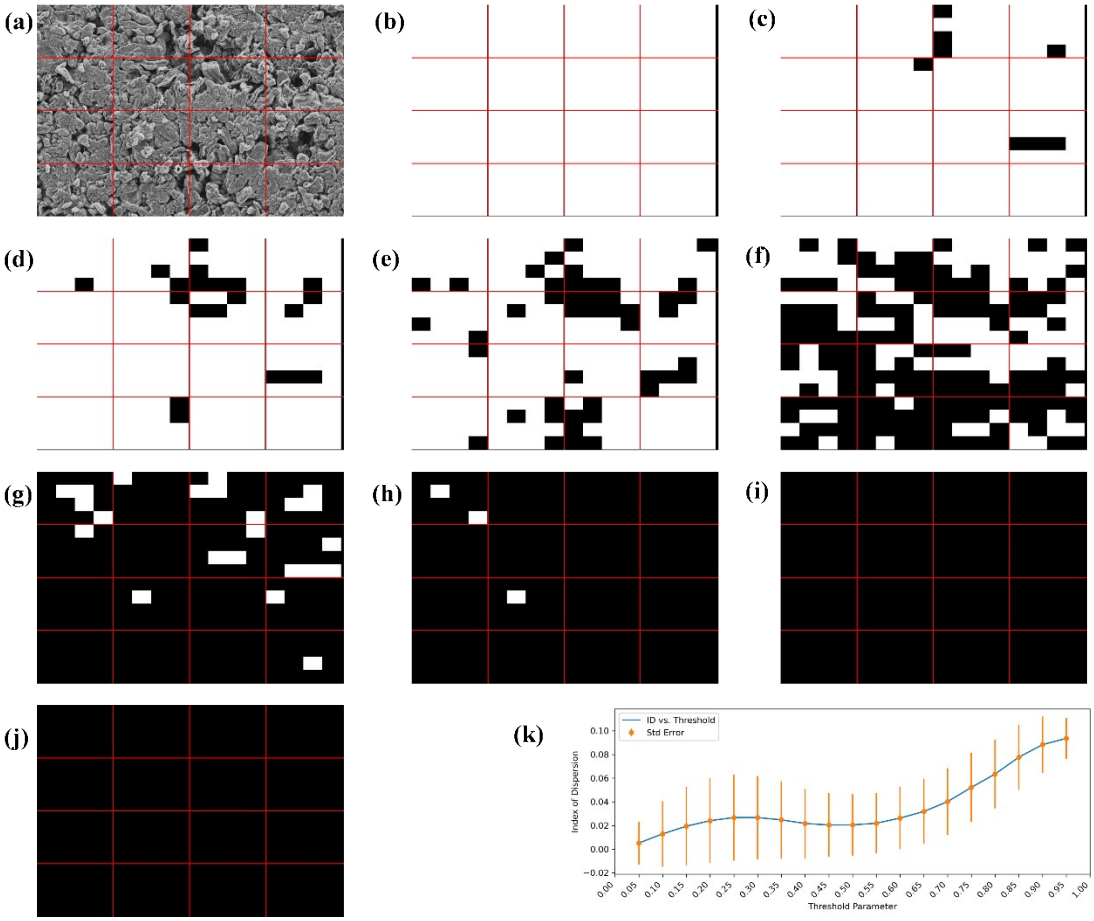

Fig. S16 (a) The SEM image 2 of the surface of lithium foil with PP separator at 100 h lithium plating under 1 mA cm^{-2} and 1 mAh cm^{-2}. (b-j) Binarization is iteratively performed starting from brightness threshold of 0.1, increasing in steps of 0.10 up to 0.90. (k) ID plotted for lithium deposition at these conditions.

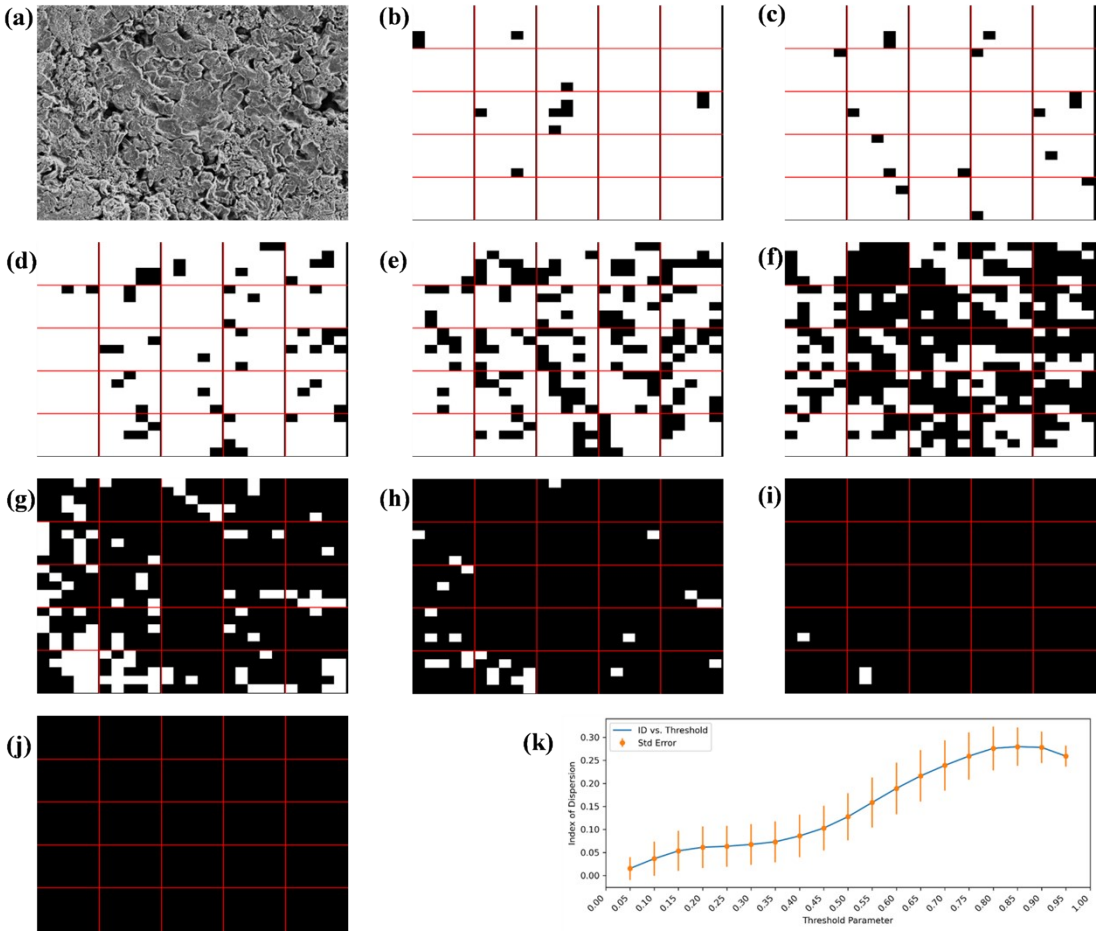

Fig. S17 (a) The SEM image 3 of the surface of lithium foil with PP separator at 100 h lithium plating under 1 mA cm^{-2} and 1 mAh cm^{-2}. (b-j) Binarization is iteratively performed starting from brightness threshold of 0.1, increasing in steps of 0.10 up to 0.90. (k) ID plotted for lithium deposition at these conditions.

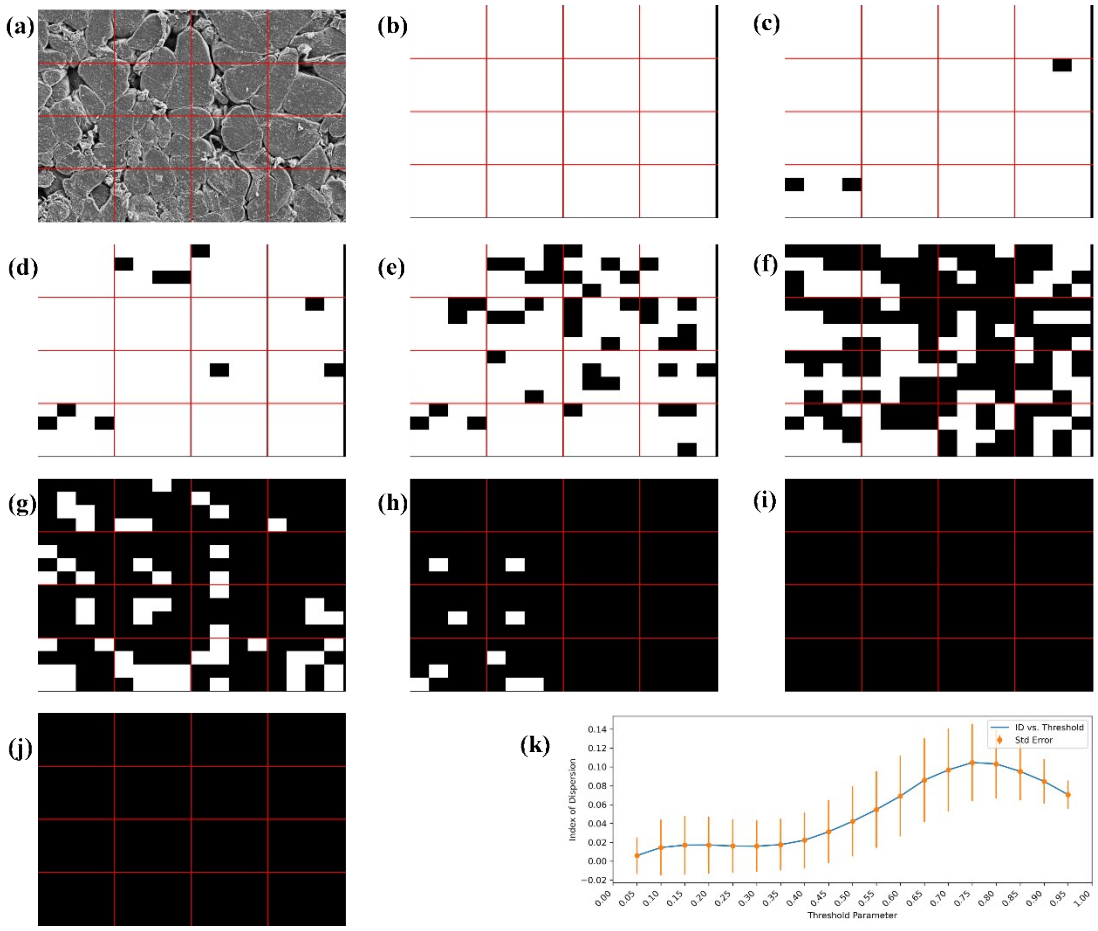

Fig. S18 (a) The SEM image 1 of the surface of lithium foil with PMA-DMAc/PP separator at 100 h lithium plating under 1 mA cm^{-2} and 1 mAh cm^{-2}. (b-j) Binarization is iteratively performed starting from brightness threshold of 0.1, increasing in steps of 0.10 up to 0.90. (k) ID plotted for lithium deposition at these conditions.

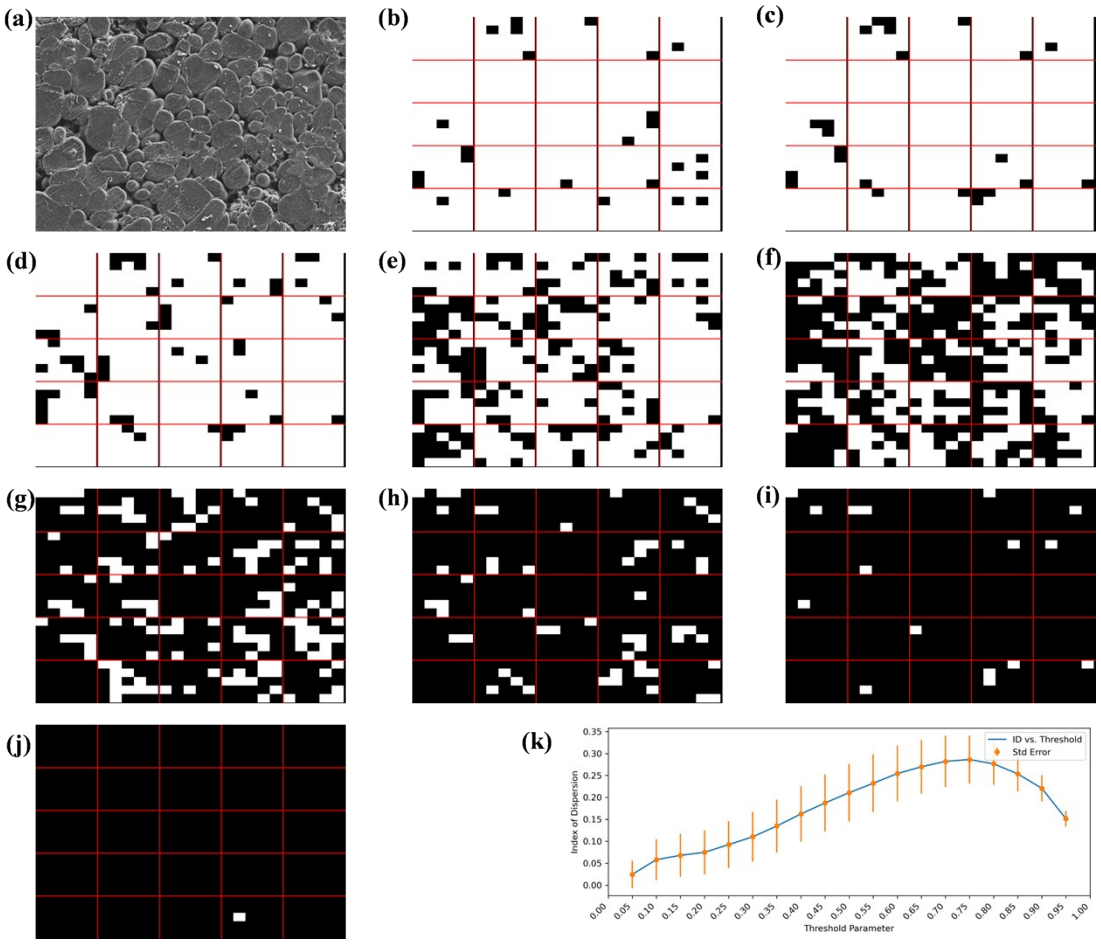

Fig. S19 (a) The SEM image 2 of the surface of lithium foil with PMA-DMAc/PP separator at 100 h lithium plating under 1 mA cm^{-2} and 1 mAh cm^{-2}. (b-j) Binarization is iteratively performed starting from brightness threshold of 0.1, increasing in steps of 0.10 up to 0.90. (k) ID plotted for lithium deposition at these conditions.

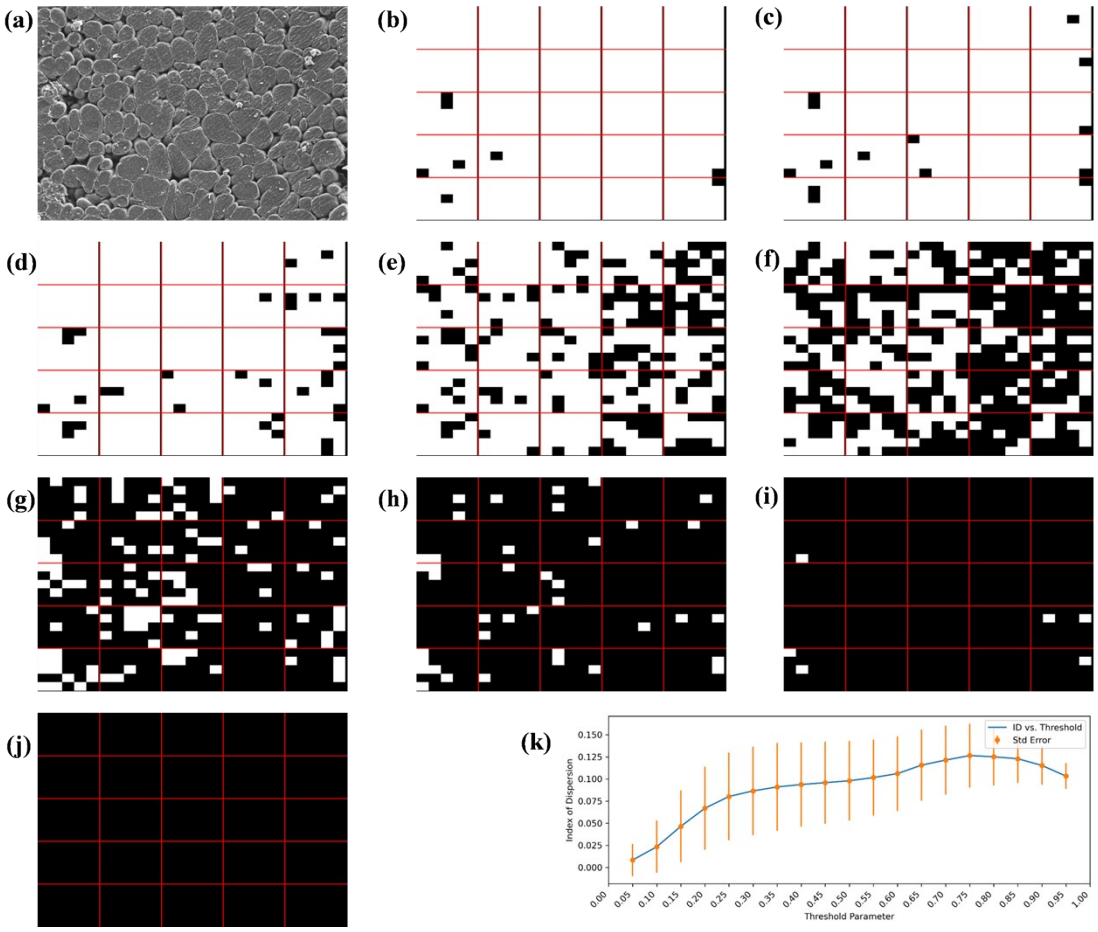

Fig. S20 (a) The SEM image 3 of the surface of lithium foil with PMA-DMAc/PP separator at 100 h lithium plating under 1 mA cm^{-2} and 1 mAh cm^{-2}. (b-j) Binarization is iteratively performed starting from brightness threshold of 0.1, increasing in steps of 0.10 up to 0.90. (k) ID plotted for lithium deposition at these conditions.

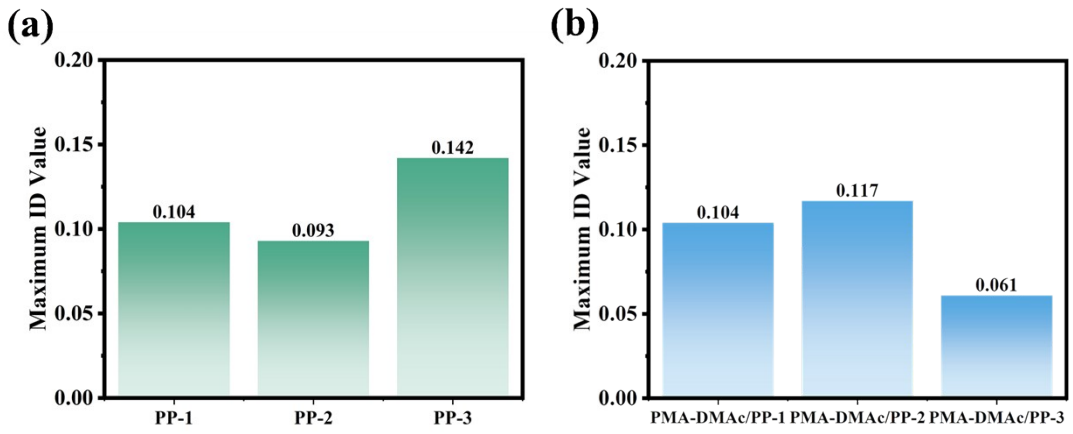

Fig. S21 The maximum ID values of the (a) pristine PP separator and (b) PMA-DMAc/PP separator.

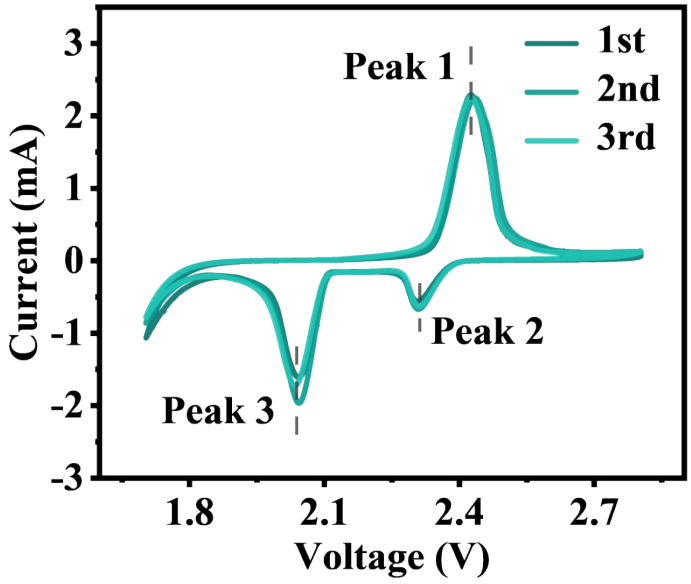

Fig. S22 CV curves of the Li-S cell with PMA-DMAc/PP separator at a scan speed of 0.1 mV s^{-1}.

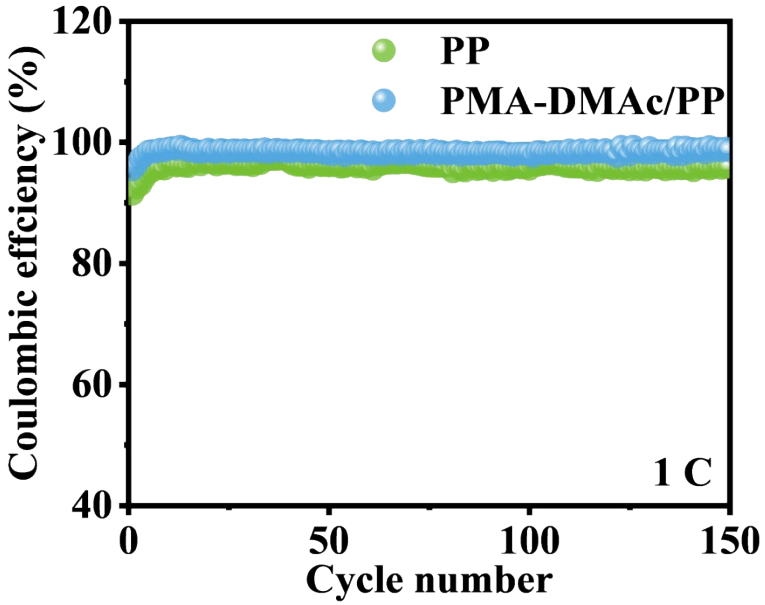

Fig. S23 Coulombic efficiency of Li-S cells with pristine PP separator and PMA-DMAc/PP separator at 1 C.

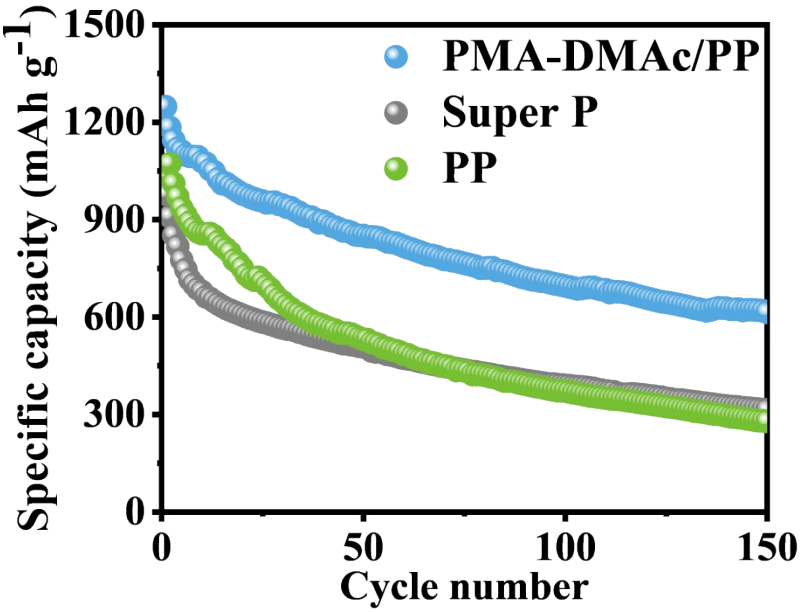

Fig. S24 Cycle performance of the cells with PMA-DMAc/PP separator, bare Super P coated separator, and pristine PP separator at 1 C.

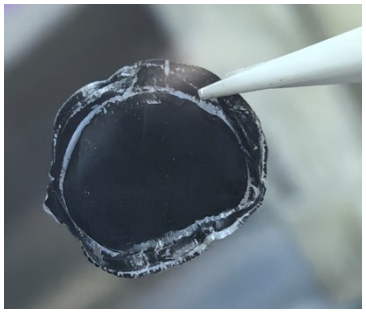

Fig. S25 Digital photograph of PMA-DMAc/PP separator after 150 cycles at 1 C.

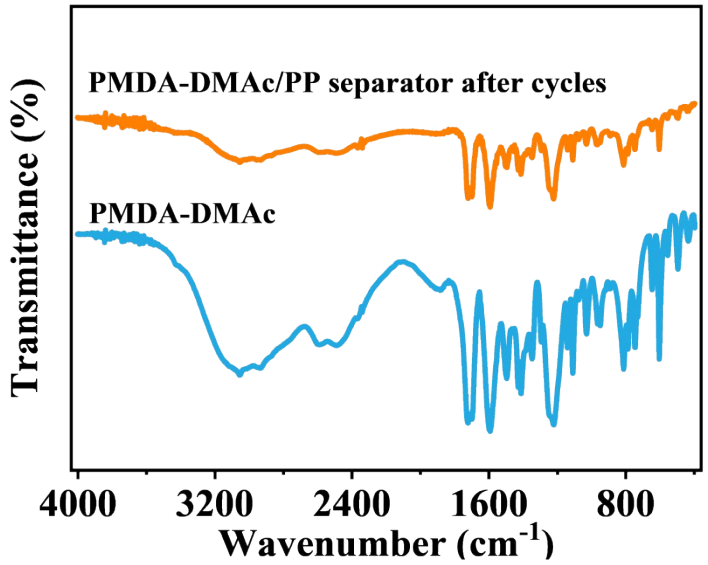

Fig. S26 FTIR spectra of PMA-DMAc crystal and PMA-DMAc/PP separator after 150 cycles at 1 C.

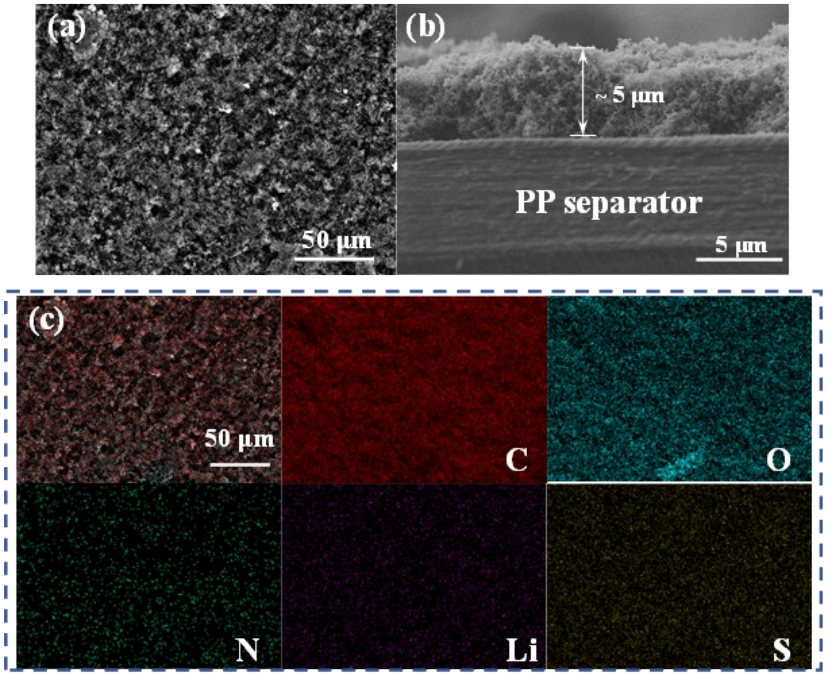

Fig. S27 The (a) top surface and (b) cross section SEM images of PMA-DMAc/PP separator after 150 cycles at 1 C. (c) The element mapping images of PMA-DMAc/PP separator after 150 cycles at 1 C.

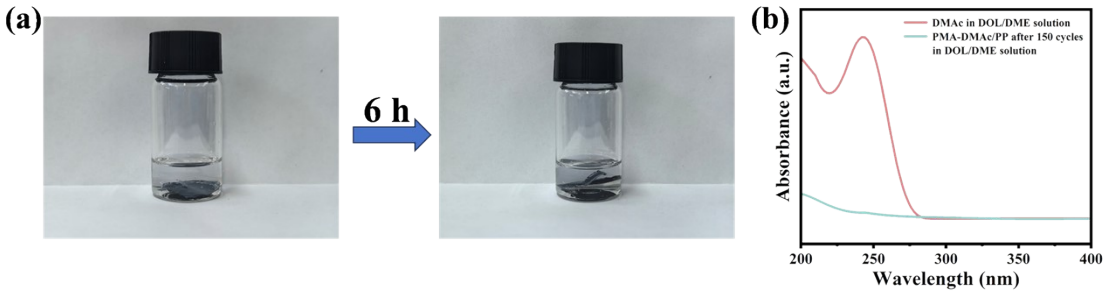

Fig. S28 (a) Observation of solubility of PMA-DMAc/PP separator after 150 cycles at 1 C. (b) UV-vis spectra of the supernatant of DOL/DME solution with PMA-DMAc/PP separator.

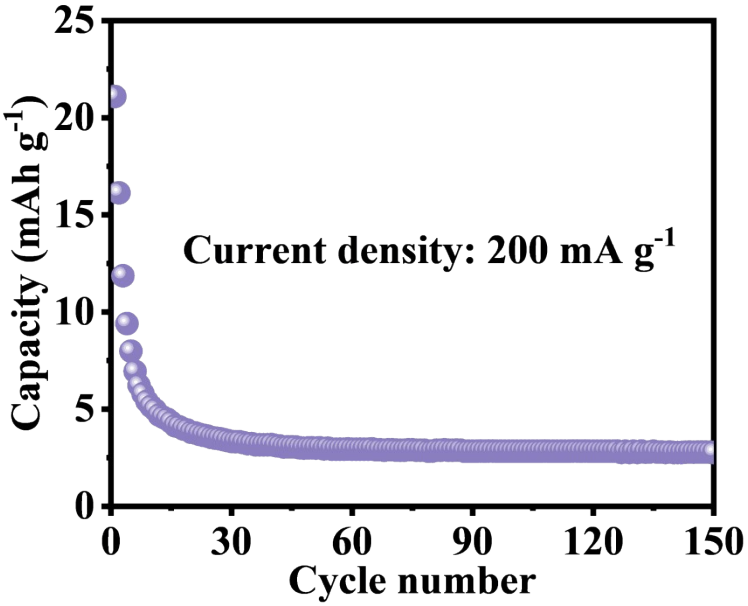

Fig. S29 Cycle performance of the cells with PMA-DMAc electrodes at the current density of 200 mA g^{-1} in the voltage range of 1.7-2.8 V. The electrode is composed of 70% active materials, 20% Super P, and 10% PVDF by weight. The electrolyte used here is the same as the Li-S cells.

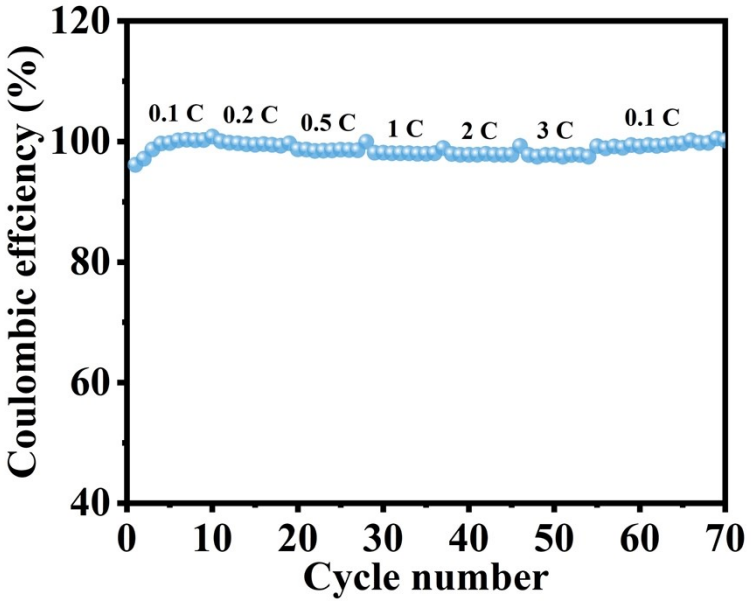

Fig. S30 Coulombic efficiency of rate performance for Li-S cell with PMA-DMAc/PP separator at current densities from 0.1 C to 3.0 C.

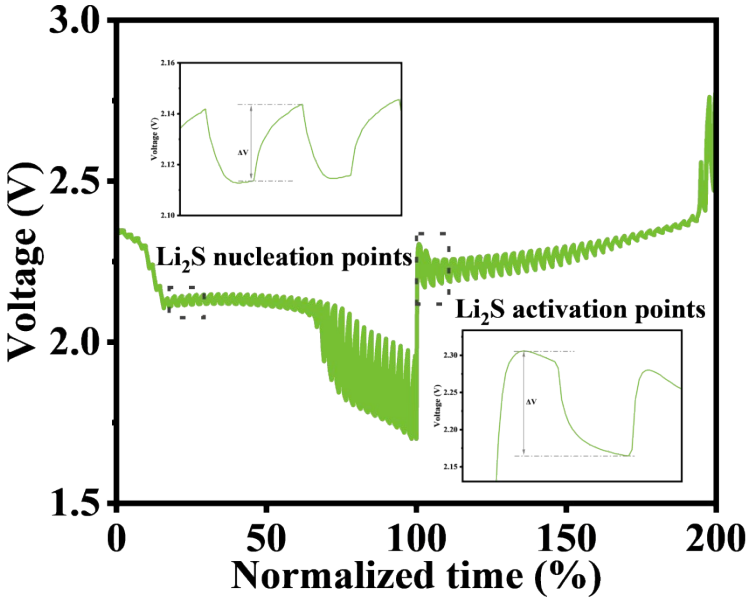

Fig. S31 GITT plot of Li-S cell with PP separator at a current density of 0.2 C.

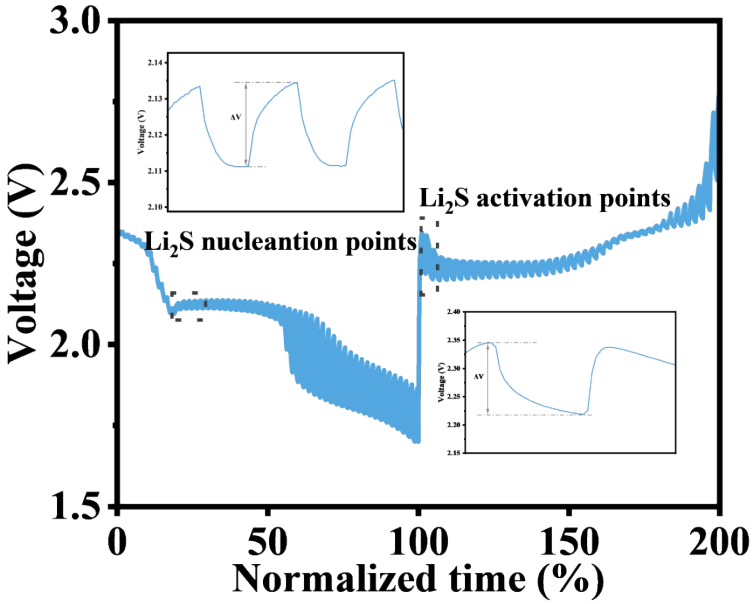

Fig. S32 GITT plot of Li-S cell with PMA-DMAc/PP separator at a current density of 0.2 C.

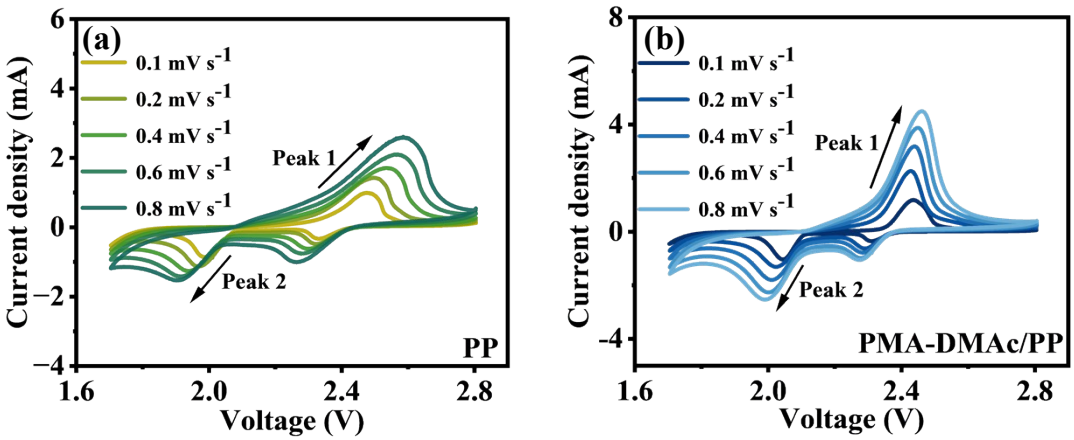

Fig. S33 CV curves of the Li-S cells with (a) PP separator and (b) PMA-DMAc/PP separator at various scan rates.

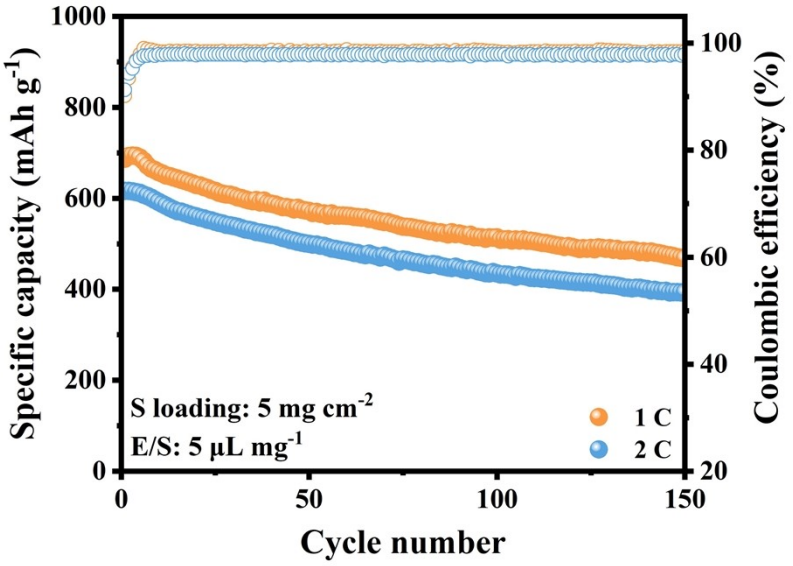

Fig. S34 Cycle performance of Li-S cells with PMA-DMAc/PP separator under sulfur loading of 5 mg cm^{-2} and E/S ratio of 5 µL mg^{-1} at 1 C and 2 C.

Table S1 Crystal data and structure refinements for {PMA-DMAc}.

Compound	**PMA-DMAc**
Empirical formula	$C_{13}H_{21}N_2O_6$
Formula weight	301.32
T (K)	273.15
Space group	*P*
Crystal system	triclinic
a / Å	7.8703(7)
b / Å	9.3910(1)
c / Å	11.0106(11)
a / °	72.161(2)
β / °	78.640(4)
γ / °	84.085(3)
V / Å^3	758.69(13)
Z	2
D_c / Mg m^{-3}	1.319
F (000)	322
Reflns collected / unique	8356 / 2399
$R_{(int)}$	0.041
Goodness-of-fit on F^2	1.133
final *R* indices	R_1[a] = 0.1041
[I>2σ (I)]	wR_2[b] = 0.2563
R indices	R_1[a] = 0.1047
(All data)	wR_2[b] = 0.2555
CCDC	2506260

[a] $R_1 = \sum||F_o| - |F_c||/\sum|F_o\}|$. [b] $wR_2 = \{\sum[w\,(F_o^2 - F_c^2)^2]/\sum[w\,(F_o^2)^2]\}^{1/2}$.

Table S2 Comparison of electrochemical performance of Li-S cell with PMA-DMAc/PP separator and other modified separators in recent literature.

Modified materials	Thickness (μm)	Sulfur loading (mg cm^{-2})	Current density	Initial capacity (mAh g^{-1})	Discharge capacity (mAh g^{-1}) after n^{th} cycle	Ref.
PMA-DMAc	5	5.0	1 C	/	475 (150th)	This work
PMA-DMAc	5	1.0	5 C	1117	470 (200th)	This work
UiO-68-BT	250	1.0	0.5 C	1063	455 (500th)	4
CON-TFSI	50	0.6	0.2 C	891	637 (500th)	5
PY-DHBD-COF	20	2.8	2 C	1266	429 (450th)	6
CoS_2-NCA@C	48	/	1 C	929	682 (90th)	7
S-MIL-125	14	2.0	0.2 C	1220	710 (200th)	8
S@COF-366-Co	/	/	0.5 C	753	493 (1000th)	9
OMC	< 50	/	0.1 C	870	574(100th)	10
GREV	/	/	0.5 C	/	707 (200th)	11
KS60	/	2.4	0.2 C	850	629 (190th)	12
NCP@PANi	20	3.1	0.5 C	713	431 (300th)	13

References

[1] G. M. Sheldrick, *SADABS, Program for Siemens Area Detector Absorption Corrections*: University of Göttingen, Germany, 1997.

[2] G. M. Sheldrick, *SHELXS 97, Program for Crystal Structure Solution*: University of Göttingen, Germany, 1997.

[3] J. R. Nicolas, Z. Hui, Q. Miao, H. Lin, M. R. Davidson and P. Liu, *Proc. Natl. Acad. Sci. U.S.A.*, 2025, **122**, e2502518122.

[4] H.-X. Li, Y.-M. Zhao, Y.-J. Wang, J.-S. Xiong, X. Du, X. Tong, J.-J. Zhang and J.-L. Zhuang, *ACS Appl. Nano Mater.*, 2025, **8**, 10944-10955.

[5] D. Ma, X. Tang, A. Niu, X. Wang, M. Wang and R. Wang, *Heliyon*, 2024, **10**, e36083.

[6] H. He, W. Wang and X. Guo, *Inorganics*, 2024, **12**, 218.

[7] J. Wang, Y. Cao, Z. Wang, Y. Zhao, C. He, F. Zhao, C. Han and S. Yu, *J. Energy Chem.*, 2024, **89**, 471-486.

[8] J. Huang, X. Jiang, P. Liu and X. Wang, *ChemistrySelect*, 2025, **10**, e01108.

[9] M. K. Shehab, M. M. Kaid, S. Pokhrel, O. K. Farha and H. M. El-Kaderi, *ACS Appl. Energy Mater.*, 2025, **8**, 12651-12660.

[10] S.-W. Seo, J.-J. Yang, Y.-S. Oh, M. Jeong, S.-J. Park and S. Ahn, *Mater. Lett.*, 2026, **404**, 139670.

[11] W. S. Heo, J. B. Park, T. Kwon, T. Lee and J. H. Lee, *Mater. Lett.*, 2026, **404**, 139640.

[12] S. Gullace, M. Abruzzese, L. Cusin, G. Saleh, S. B. Thorat, A. Gamberini, S. Bellani, A. Ciesielski, F. Bonaccorso and P. Samorì, *J. Mater. Chem. A*, 2024, **12,** 25359-25370.

[13] Z. Li, Y. Wang, B. Wang, H. Su, Y. Shang and H. Liu, *New J. Chem.*, 2024, **48**, 5289-5299.